Adjusting the Redox Coupling Effect via Li/Co Anti-Site Defect for Stable High-Voltage $LiCoO_2$ Cathode

Weijin Kong[a], Dong Zhou[b], Qinghua Zhang[c], Deniz Wong[d], Ke An[e], Christian Schulz[d], Nian Zhang[f], Jicheng Zhang[a*] and Xiangfeng Liu[a,g*]

[a] Center of Materials Science and Optoelectronics Engineering, College of Materials Science and Optoelectronic Technology, University of Chinese Academy of Sciences, Beijing 100049, P. R. China

[b] Institute of Advanced Science Facilities, Shenzhen, Guangdong, 518107, P. R. China

[c] Beijing National Laboratory for Condensed Matter Physics, Institute of Physics, Chinese Academy of Science, Beijing, P. R. China

[d] Dynamics and Transport in Quantum Materials, Helmholtz-Zentrum Berlin für Materialen und Energie, Albert-Einstein-Strasse 15, 12489 Berlin, Germany.

[e] Neutron Scattering Division, Oak Ridge National Laboratory, Oak Ridge, Tennessee, 37830, USA

[f] Shanghai Institute of Microsystem and Information Technology, Chinese Academy of Science, Shanghai 200050, P. R. China

[g] CAS Center for Excellence in Topological Quantum Computation, University of Chinese Academy of Sciences, Beijing 100190, China

*Corresponding Author: liuxf@ucas.ac.cn. (X.L.) Tel. +86 10 8825 6840;

zhangjc@ucas.ac.cn (C. Z.)

Abstract

High-voltage $LiCoO_2$ is pressingly required for the portable electronics. But the O→Co charge transfer and the oxygen redox at high delithiation induce the issues of irreversible Co reduction, oxygen release and unfavored phase transformation. Herein, we propose to tune the O→Co charge transfer via regulating Li/Co anti-site defect with Mg^{2+} and $(PO_4)^{3-}$ co-doping to achieve a stable high-voltage $LiCoO_2$ cathode. The appropriately regulated Li/Co anti-site defect enhances the redox activity of the Co-ions, inhibits the redox activity of the oxygen and the coupled Co reduction. The increase of the formation energy of oxygen vacancies in the modified cathode at deep delithiation inhibits oxygen escape. Moreover, $(PO_4)^{3-}$ doping also stabilizes oxygen-packed framework due to its strong bond energy with transition metal. These functions enhance the structural stability and the reversible Co/O redox ability. The improved cathode delivers a high capacity and long-cycle capacity retention on both 4.5 V and 4.6 V. This study provides some insights into adjusting the redox coupling effect and enhancing the oxygen redox reversibility by Li/Co anti-site regulation.

Key words: Li/Co anti-site, high voltage $LiCoO_2$, redox coupling, formation energy, oxygen escape

TOC

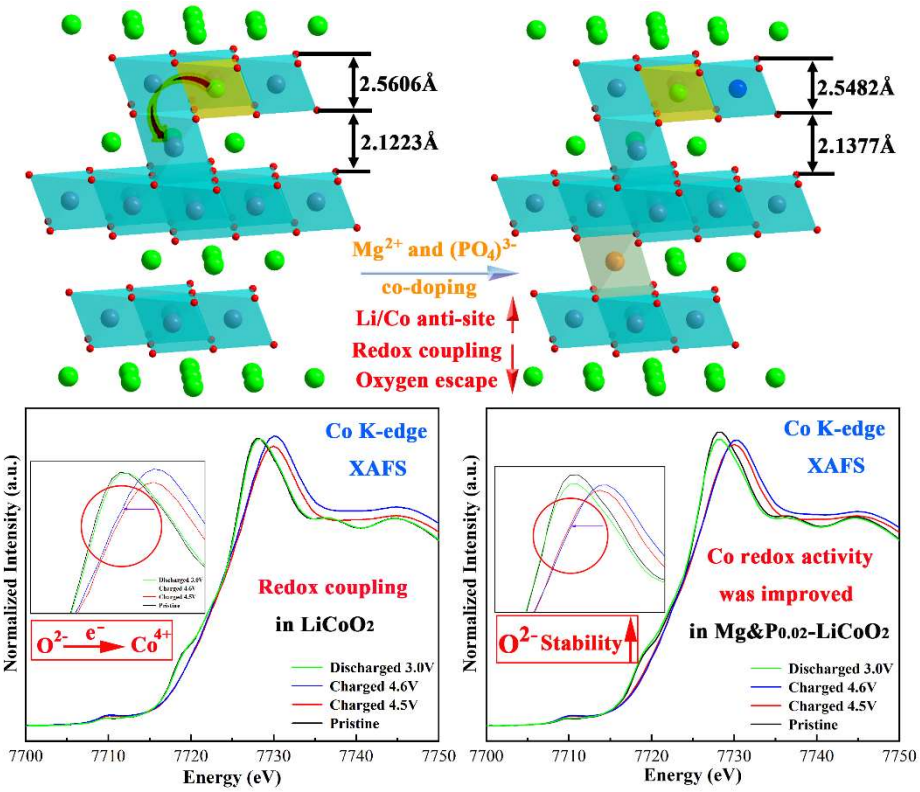
2.5606Å
2.1223Å
2.5482Å
2.1377Å
Mg2+ and (PO4)3-
co-doping
Li/Co anti-site
Redox coupling
Oxygen escape
Co K-edge
XAFS
Redox coupling
in LiCoO2
O2- e- Co4+
Discharged 3.0V
Charged 4.6V
Charged 4.5V
Pristine
Normalized Intensity (a.u.)
Energy (eV)
7700
7710
7720
7730
7740
7750
Co K-edge
XAFS
Co redox activity
was improved
in Mg&P0.02-LiCoO2
O2- Stability
Discharged 3.0V
Charged 4.6V
Charged 4.5V
Pristine
Normalized Intensity (a.u.)
Energy (eV)

1. Introduction

The rechargeable lithium-ion batteries (LIBs) with high safety and high specific energy are pressingly required for the rapid development of consumer electronics, electric vehicles and energy storage [1]. At present, advanced cathode is the bottleneck for the exploration of high specific energy LIBs[2]. Due to the good conductivity, superior high volume energy density and theoretical capacity, $LiCoO_2$ has been regarded as the ideal cathode for 3C electronics and has attracted wide attention[3]. However, the practical reversible capacity of common $LiCoO_2$ is only half of its theoretical capacity (274 mAh/g). To elevate the delivered capacity, a high voltage ceiling is inevitable [4]. With a 4.6V upper voltage limit, the capacity is up to 220 mAh/g. But this would induce significant structural degradation, oxygen release, cation dissolution and the sharp capacity decay[5]. In addition, with the increasing of charging voltage, when the electrons at the top of the Co elements valence band are depleted, the charge compensation process in this region will no longer be provided by the Co-ions, and the anionic oxygen will also participate in it due to the overlap between Co_{3d} band and O_{2p} band (strong covalence of the Co-O bond)[6]. The high activity and mobility of the peroxide ion O^- at the high voltage can not only easily escape from the crystal in the form of the O_2 gas, but also leads to the electrolyte oxidation and decomposition rapidly increased, causing the large interfacial impedance and severe gas generation.[7]

These issues are related with the redox mechanism of $LiCoO_2$. When the charge voltage exceeds 4.2V, the conventional $Co^{3+/4+}$ oxidation is changed to the reactions involving both Co cations and O anions[8]. The O anionic redox elevates the capacity,

but complicates the reactions and bring problems. Specifically for the whole delithiating, charge compensation only takes place in Co dominated t_{2g} band when it is below a 4.2V charge voltage, while which correlate the O_{2p} band at voltages higher than 4.2V. A series of phenomena have been observed. It is reported that the structural degradation is occurred in the delithiated $LiCoO_2$ at high-voltages, which induces phase transition from layered to spinel structure[9]. Simultaneously, $Co^{3+/2+}$ reduction and oxygen release are companied[10]. In this process, Co^{2+} ions will occupy the tetrahedral position of Li^+, which hinder the Li^+ migration.

In addition, the Li/Co anti-site defect usually occurs during the electrochemical cycle, because of a similar ion radius (Co^{2+}: 0.0745Å, Co^{3+}: 0.061Å, Li^+: 0.076Å). The migration and dissolution of Co ions will lead to the change of the layered structure from the surface to the interior or the phase transition. And for the anti-site Li-ions in transition metal Co site will improve the stability of oxygen framework due to the enhanced Li-O interaction[11]. Besides, in some cases, the O^{2-} to $O^{(2-n)-}$ process often accompanied with the reduction of the Co ions under high voltage. In other words, during the deep charging process, to reduce the energy of the whole system, some electrons in the high O_{2p} occupied state flowing to the Co_{3d} unoccupied state, which is called the redox coupling mechanism[12]. Therefore, studying the effect of the Li/Co anti-site defects on the structure and electrochemical performance of high-voltage $LiCoO_2$ cathode materials, as well as in-depth understanding of the evolution of transition metal Co ions and oxygen ions in the charging/discharging cycles and the redox coupling effect of cationic Co ions are particularly important for designing high-

performance high-voltage $LiCoO_2$ cathode materials.

Herein, we proposed a facile strategy to regulate the Li/Co anti-site defect through Mg^{2+} and $(PO_4)^{3-}$ co-doping and improve the redox activity of Co ion as well as inhibit the redox coupling in $LiCoO_2$ cathode materials. And the formation energy of oxygen vacancies was enhanced by the Mg^{2+} and $(PO_4)^{3-}$ co-doping at deep delithiation. Therefore, Li/Co anti-site defect regulation further reduces the redox activity of O^{2-} ions and enhances the redox reversibility of O^{2-} ions, especially under a high voltage. The intrinsic mechanism was revealed by combining the powered neutron diffraction (NPD), differential electrochemical mass spectrometry (DEMS), the X-ray absorption fine structure spectra(XAFS), the resonant inelastic X-ray scattering (RIXS) and the first principles calculations (DFT). This strategy might be also extended to other cathode materials related to the oxygen redox.

2. Result and Discussion

Crystal structure and Morphology

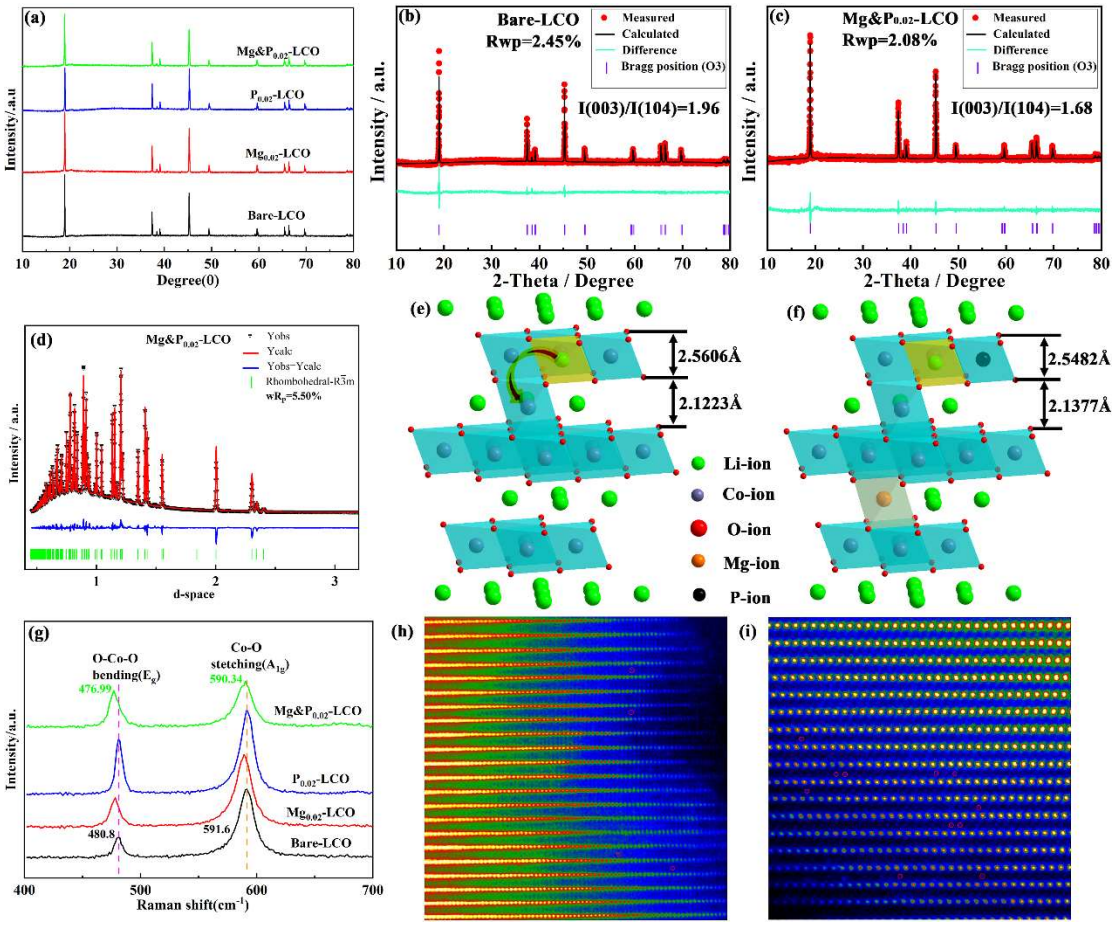

Figure 1. the structural characterization of the Bare-LCO, $Mg_{0.02}$-LCO, $P_{0.02}$-LCO and Mg&$P_{0.02}$-LCO samples: (a) the XRD patterns; the refinement results of the XRD: (b) Bare-LCO, (c) Mg&$P_{0.02}$-LCO, and the refinement results of the neutron powder diffraction (NPD): (d) Mg&$P_{0.02}$-LCO, the Refined crystal structures: (e) Bare-LCO and (f) Mg&$P_{0.02}$-LCO by the XRD, (g) the Raman patterns of the Bare-LCO, $Mg_{0.02}$-LCO, $P_{0.02}$-LCO and Mg&$P_{0.02}$-LCO cathode materials, HAADF-STEM images of the (h) Bare-LCO and (i) Mg&$P_{0.02}$-LCO cathode materials along the [110] direction, respectively, which represent the Li/Co anti-site

In order to reveal the crystal structures of the Bare-LCO, $Mg_{0.02}$-LCO, $P_{0.02}$-LCO and Mg&$P_{0.02}$-LCO cathode materials, the X-ray diffraction (XRD) was tested as shown in Figure1 (a), and all the diffraction peaks of both samples can be consistent with the rhombohedral structures in the $R\bar{3}m$ space group symmetry[4b, 13], which also

proved that the bulk crystal structure of the $LiCoO_2$ cathode materials was not much changed by the Mg^{2+} and $(PO_4)^{3-}$ doping. In order to reveal the effect of the Mg^{2+} and $(PO_4)^{3-}$ doping on the crystal structure parameters, the Rietveld refinement of the XRD patterns of the four samples and the NPD patterns of the Bare-LCO and Mg&$P_{0.02}$-LCO cathode materials were performed as shown in Figure 1 (b), (c), (d) and Figure S1. Compared with the Bare-LCO cathode material, the I(003)/I(104) value of the Mg&$P_{0.02}$ cathode material was decreased from 1.96 to 1.68 as shown in Figure1 (b) and (c), which illustrate that the suitable increase of the Li/Co anti-site by the Mg^{2+} and $(PO_4)^{3-}$ co-doping[14]. The occupancy information of the atoms in the cathode materials derived from the Rietveld refinement by XRD and NPD are depicted in Tables S1~S6, respectively. Compared with the Bare-LCO cathode materials, the Li/Co anti-site was appropriately increased in the Mg&$P_{0.02}$-LCO cathode materials by the NPD patterns as shown in Table S5 and Table S6. The refined crystallographic parameters are listed in Table 1(by XRD). The fitting factors R_{wp} from the XRD patterns are 2.45 and 2.08%, respectively, which mean that the refined data are acceptable for further reference[15].

Table 1 The refined crystallographic parameters of the cathode materials by the XRD patterns

Sample	a(Å)	c(Å)	V(Å^3)	Z_{ox}	TM-O	$S_{(MO2)}$(Å)	$I_{(LiO2)}$(Å)	R_{wp}(%)
Bare LCO	2.8154(0)	14.0487(3)	96.43(0)	0.2422(8)	1.9412	2.5606	2.1223	2.45
Mg&$P_{0.02}$-LCO	2.8142(1)	14.0578(2)	96.42(0)	0.2427(5)	1.9448	2.5482	2.1377	2.08

Moreover, the crystal structure of the Bare-LCO and Mg&$P_{0.02}$-LCO cathode materials based on the Rietveld refinement of the XRD pattern are shown in Figure 1 (e) and (f). Compared with the Bare-LCO cathode materials (2.1223 Å), the interlayer

space of the Mg&$P_{0.02}$-LCO cathode material was significantly expanded to 2.1377 Å, which can provide a wider channel for Li^+ intercalation/extraction during the charge/discharge processes and further lower the energy barrier and the resistance of Li^+ migration. This result will be beneficial to the improvement of the rate capacity[16]. In addition, the shift of the strong Raman bonds to the left for the $Mg_{0.02}$-LCO and Mg&$P_{0.02}$-LCO cathode materials indicates the existence of the lithium vacancies due to the substitution of Mg^{2+} for Li^+ and the Li/Co anti-site, which also confirms that the Mg^{2+} enter to the Li^+ site without changing the layered structure of the cathode materials. In order to observe the phenomenon of the Li/Co anti-site more intuitively, the HAADF-STEM images of both samples were performed as shown in Figure1 (h) and (i). Compared with the Bare-LCO cathode material in Figure 1 (h), the phenomenon of the Li/Co anti-site was appropriately increased by the Mg^{2+} and $(PO_4)^{3-}$ co-doping, which is consistent with the decreased I(003)/I(104) value. Moreover, the Li/Co anti-site defect has increased in a certain range, which will be conducive to the improvement of the long-term cycle stability of the cathode materials, although it is not conducive to the enhancement of the initial capacity.

Figure S2 shows the Co-$L_{3,2}$ SXAS spectra of the Bare-LCO, $Mg_{0.02}$-LCO, $P_{0.02}$-LCO and Mg&$P_{0.02}$-LCO samples in TEY model, and the positions of the main peaks of the four samples are basically at the same energy, and there is no obvious change. But in Figure S3, in combination with the soft XAS spectra of the O in TEY mode, the difference between the four samples lies in the obvious change of the back edge peak of O at about 530 eV, which indicates that the coordination environment of O has

changed slightly[17]. Therefore, it can confirm that the Mg^{2+} and $(PO_4)^{3-}$ play functions in influencing the electronic structure. The X-ray photoelectron spectroscopy (XPS) was used to analyze and determine the surface chemical state and valence information of the element on the surface of the four samples as shown in Figure S4. The main peak of the Mg1s is located at about 1303 eV as shown in Figure S4 (c), which indicates that the Mg^{2+} exists in $Mg_{0.02}$-LCO and Mg&$P_{0.02}$-LCO cathode materials[18]. In addition, the main peak of the P_{2p} is located at about 131 eV as shown in Figure S4 (d), combined with the 3D representation of the TOF-SIMS depth profile as shown in Figure S5, which confirms that there are $(PO_4)^{3-}$ ions doped into the $P_{0.02}$-LCO and Mg&$P_{0.02}$-LCO cathode materials[19].

The high-resolution transmission electron microscopy (HRTEM) images and selected area electron diffraction (SAED) patterns of the samples before and after modification are performed (Figure S6). Compared with the Bare-LCO, Mg&$P_{0.02}$-LCO exhibits a larger (104) spacing. This provides larger space for the migrated Co cations. In order to observe the distribution of each element in the Mg&$P_{0.02}$-LCO cathode material, the EDS mapping was performed as shown in Figure S6 (e)~(j), showing uniform distributions of the Co, Mg, P, O elements.

Electrochemical performances and mechanisms

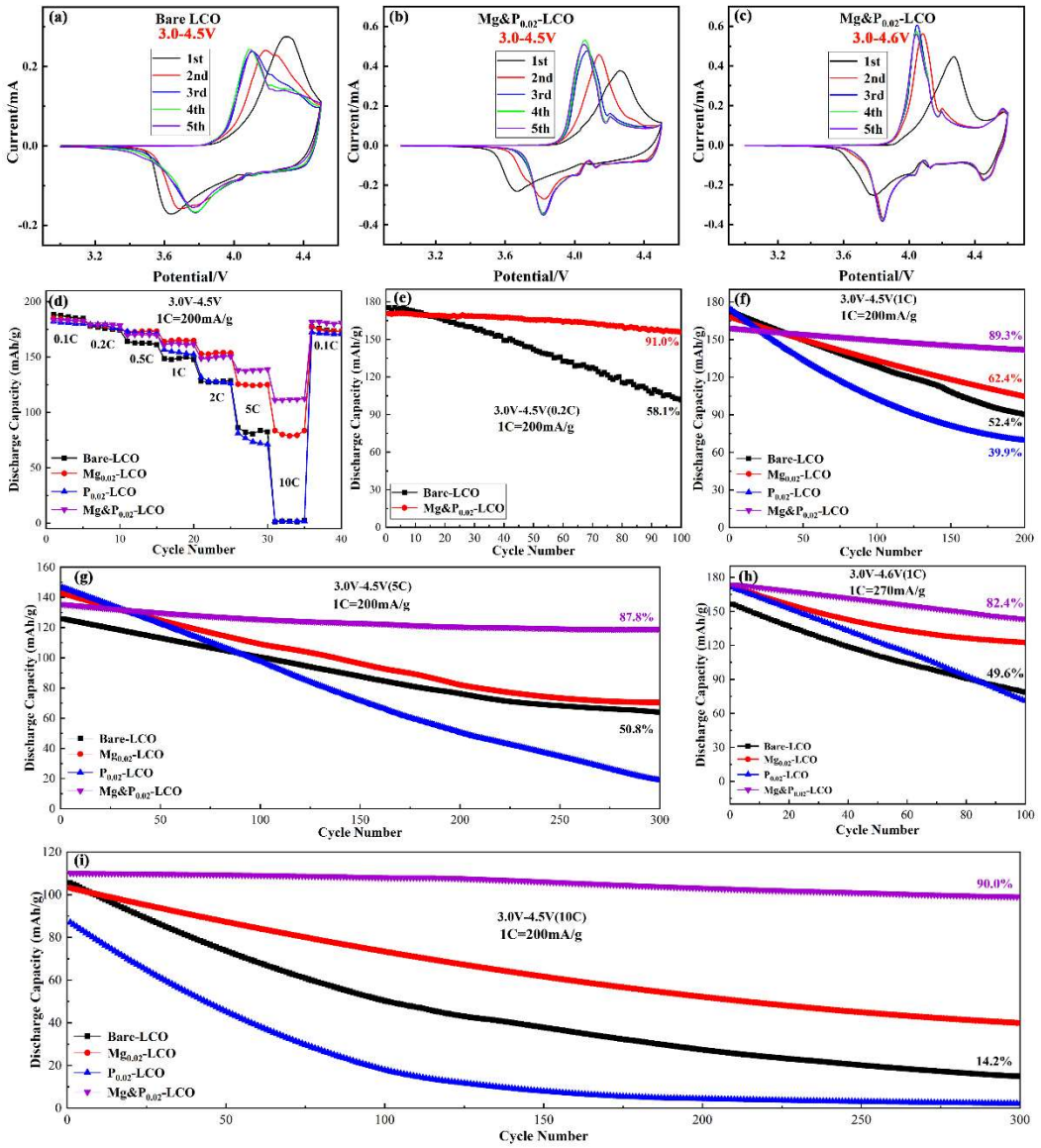

Figure 2. the Cyclic Voltammetry (CV) curves of as-prepared electrode materials with the scan rate of 0.1 mV/s from 3.0V to 4.5V: (a) Bare-LCO and (b) Mg&$P_{0.02}$-LCO samples, (c) the Cyclic Voltammetry (CV) curves of Mg&$P_{0.02}$-LCO samples with the scan rate of 0.1mV/s from 3.0V to 4.6V, Rate capabilities and cycle performance test at different current densities (Bare-LCO, $Mg_{0.02}$-LCO, $P_{0.02}$-LCO and Mg&$P_{0.0}$-LCO; 1C = 200 mA/g) from 3.0V to 4.5V, (d) rate capabilities, cycling performance at (e) 0.2C, (f) 1C, (g) 5C and (i) 10C (The loaded mass of the active materials is about 2.0 mg/cm^2, namely, ~0.4mAh/cm^2), (h) cycle performance test of Bare-LCO, $Mg_{0.02}$-LCO, $P_{0.02}$-LCO and Mg&$P_{0.02}$-LCO samples at 1C (1C = 270 mA/g) from 3.0V to

4.6V

To better reveal the redox peaks, the kinetics and phase transition of the Bare-LCO, $Mg_{0.02}$-LCO, $P_{0.02}$-LCO and Mg&$P_{0.02}$-LCO cathode materials, the cyclic voltammetry (CV) was performed with the voltage range of 3.0V-4.5V as shown in Figure 2 (a), (b) and Figure S7. Compared with the Bare-LCO cathode materials, the polarization phenomenon of the Mg&$P_{0.02}$-LCO sample was obviously reduced. In addition, the CV plot of the Mg&$P_{0.02}$-LCO sample with the voltage range of 3.0V-4.6V demonstrates a stable electrochemical reaction. Besides, the increasing sharp peaks of Co redox at about 4.1V and the reduced polarization phenomenon of Mg&$P_{0.02}$-LCO declare an enhanced Co redox.

As shown in Figure 2 (d), the rate performance of Bare-LCO, $Mg_{0.02}$-LCO, $P_{0.02}$-LCO and Mg&$P_{0.02}$-LCO were investigated in a range of 3.0V~4.5V. Mg&$P_{0.02}$-LCO shows superior rate performance, delivering capacities of 183, 179, 170, 162, 150, 138 and 112 mAh/g at 0.1C, 0.2C, 0.5C, 1C, 2C, 5C and 10C (1C=200 mA/g), respectively. In contrast, the Bare-LCO samples show a worse rate capacity with corresponding discharging capacities of 188, 178, 164, 149, 129, 86 and 1 mAh/g at 0.1C, 0.2C, 0.5C, 1C, 2C, 5C and 10C, respectively. The improvement of the rate performance benefits from the expansion of the interlayer $I_{(LiO2)}$ in the layered structure, because the positive impact of Mg^{2+} and $(PO_4)^{3-}$ ions co-doping on the host structure, which can provide a stable and wide channel for the fast migration of Li ions.

Long-term cyclic stability is the evaluation standard that can best reflect the performance of the cathode materials, so the cycle performance of the four samples at

0.2C, 1C, 5C and 10C (1C=200 mA/g) have been tested at the range of 3.0-4.5V as shown in Figure 2 (e)-(g) and (i). Compared with the Bare-LCO cathode material, the initial capacity of the Mg&P$_{0.02}$-LCO sample is slightly reduced. However, the long-term cycle stability was largely enhanced, and the capacity retention has been considerably improved under both the small and large current density during the charging/discharging process. The charge/discharge curves of both samples at 0.1C and 1C are shown in Figure S9. In order to further test the impact of the Mg^{2+} and $(PO_4)^{3-}$ ions co-doping on cycle stability under a much higher voltage of 4.6V, the electrochemical performance of four samples was tested under 1C (1C=270 mA/g), as shown in Figure 2 (h). After 100 cycles, the capacity retention was increased from 49.6% for Bare-LCO to 82.4% for Mg&P$_{0.02}$-LCO.

To further reveal the modifications in electrochemical performance for Mg&P$_{0.02}$-LCO, the electrochemical impedance spectroscopy (EIS) and the potentiostatic intermittent titration technique (PITT) were performed, as shown in Figure S8(a) to (d). Compared with the Bare-LCO, the values of R_s and R_p are much smaller for the Mg&P$_{0.02}$-LCO sample. And the Li^+ diffusion coefficient is also improved. Besides, the energy barriers of Li^+ migration for both samples were calculated by the DFT calculations (Figure S8e). Compared with the Bare-LCO (0.39 eV), the Li^+ migration barrier of the Mg&P$_{0.02}$-LCO cathode material was decreased to 0.33 eV, which illustrates a fast Li^+ diffusion in Mg&P$_{0.02}$-LCO, corresponding to the improvement in the rate performance.

Electronic Structure Analysis

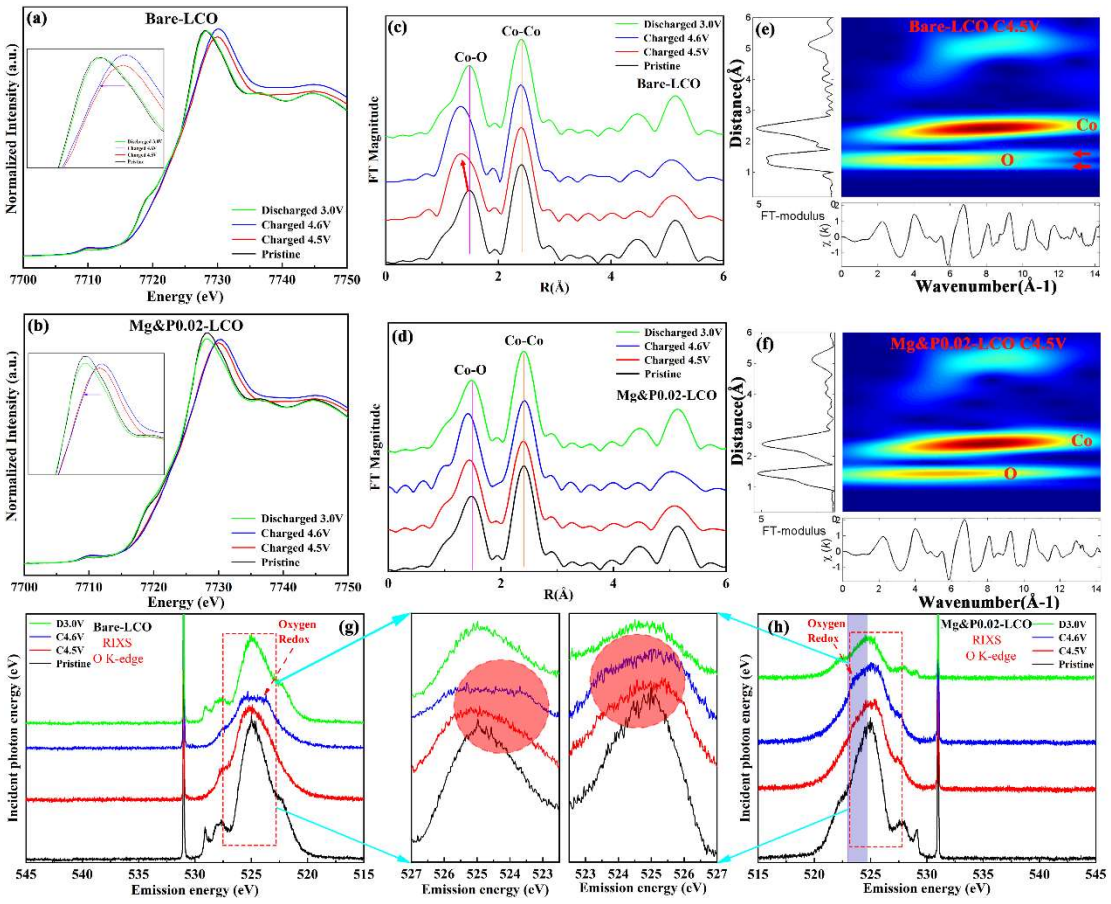

Figure 3. The normalized Co K-edge of the (a) Bare-LCO samples, (b) Mg&P$_{0.02}$-LCO samples, the Fourier-transformed Co K-edge XAFS: (c) Bare-LCO samples, (d) Mg&P$_{0.02}$-LCO samples, the wavelet transform of Co K-edge XAFS at charged 4.5V state: (e) Bare-LCO samples, (f) Mg&P$_{0.02}$-LCO samples, the oxygen RIXS O K-edge of the (g) Bare-LCO samples and (h) Mg&P$_{0.02}$-LCO samples with the excitation energy of 531 eV

In order to research the evolution of the electronic and local structure of the bulk Co, the ex-situ XAFS is adopted in Figure 3(a) and (b). The pre-edge and the edge declare the specific structural information, which reflects the valence change of Co ions during the charging/discharging process. As shown in Figure 3(a), for Bare-LCO, compared with that in the spectrum for 4.5V electrode, the Co K-edge in the spectrum for 4.6V electrode is slightly shifted to the lower energy. This declares a reducing Co

valence state for the Bare-LCO electrode is charged from 4.5V to 4.6V states. This is related with the coupling Co reduction when O redox is occurred. While there is no similar phenomenon occurs in the Mg&P$_{0.02}$-LCO sample as shown in Figure 3(b), which indicate that the redox activity of the Co ions was improved by the Mg^{2+} and $(PO_4)^{3-}$ ions co-doping. The differences between Bare-LCO and Mg&P$_{0.02}$-LCO manifest different redox mechanisms, especially for the O→Co charge transfer at 4.6V.

To better reflect the change of coordination environment between Co and oxygen, the Fourier-transformed and wavelet transform of Co K-edge XAFS was carried out as shown in Figure 3(b), (c), (e), (f) and Figure S10. Compared with Bare-LCO, Mg&P$_{0.02}$-LCO expresses a reduced Co-O bond length change from the pristine to charged states, which is evidenced by the alleviative Co-O shell shift. [20] Through wavelet transform as shown in Figure 3(e) and (f), the signal of Co-O shell for Bare-LCO is split at charged 4.5 V state, in contrast, the Mg&P$_{0.02}$-LCO electrode maintains one Co-O shell form, which indicate a varied structure change of materials. These results may come from the different oxygen redox reactions in two materials.

In order to effectively reveal the oxygen redox chemistry under different charging states in both Bare-LCO and Mg&P$_{0.02}$-LCO electrodes, the O K-edge RIXS was carried out as shown in Figure 3(g) and (h). Both the Bare-LCO and Mg&P$_{0.02}$-LCO samples show similar spectra shapes in their pristine and discharge states. The peak at about 523 eV in O K-edge RIXS spectra is regarded as the O redox feature.[21] While in the charged state, the O redox featured peak is more obvious for Bare-LCO than Mg&P$_{0.02}$-LCO, This indicates that the irreversibility oxygen redox is restrained in

Mg&P$_{0.02}$-LCO cathode. This is helpful to enhance the structural stability of the cathode material at high voltage, especially at 4.6V. This result is consistent with the Co K-edge XAFS spectra, which further supports the idea that the O→Co charge transfer is alleviated in Mg&P$_{0.02}$-LCO at high voltages.

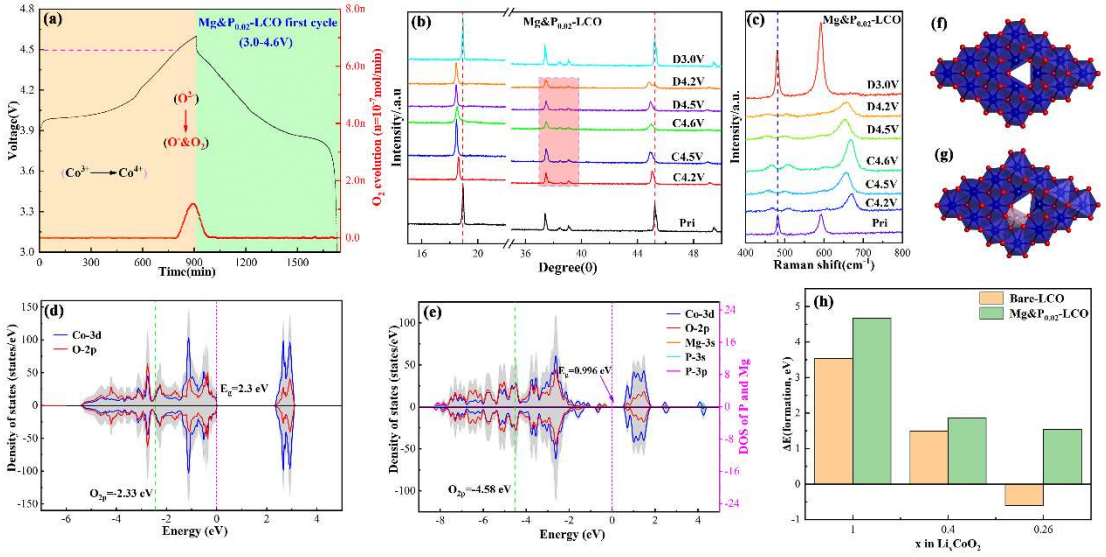

Figure 4. (a) the operando DEMS of the Mg&P$_{0.02}$-LCO samples at the current density is 0.05C, the active materials of Mg&P$_{0.02}$-LCO samples is 16.48mg, (b) the *Ex-situ* XRD patterns of the Mg&P$_{0.02}$-LCO sample; (c) the *Ex-situ* Raman patterns of the Mg&P$_{0.02}$-LCO sample, the calculated total and partial density of states (DOS) of the (d) Bare LCO, (e) Mg&P$_{0.02}$-LCO the oxygen vacancy formation in deep delithiation state (f) Bare LCO, (g) Mg&P$_{0.02}$-LCO; the oxygen vacancy formation energies of the (h) Bare LCO and Mg&P$_{0.02}$-LCO

Moreover, operando differential electrochemical mass spectrometry (DEMS) measurements of the initial charge/discharge processes for the Bare-LCO and Mg&P$_{0.02}$-LCO samples were conducted. The O_2 gas loss for samples upon charge/discharge is declared in Figure 4 (a) and Figure S11 (a). Compared with the

Bare-LCO, the O_2 release is obvious inhibited for Mg&P$_{0.02}$-LCO. This result is consistent with above results on revealing the inhibition of the oxygen redox in Mg&P$_{0.02}$-LCO.

Combined with the Co K-edge XAFS and the O K-edge RIXS data, it includes that Mg&P$_{0.02}$-LCO has an enhanced Co redox and oxygen redox reversibility[22]. This is rooted with the Li/Co disorder which is caused by Mg^{2+} and $(PO_4)^{3-}$ ions co-doping. At the functions of modulated charge transfer, the capacity contributed by $Co^{3+/4+}$ redox is larger for Mg&P$_{0.02}$-LCO than Bare-LCO. While the capacity contributed by O redox is smaller for Mg&P$_{0.02}$-LCO than Bare-LCO. The tuned Co/O redox behaviors benefits Mg&P$_{0.02}$-LCO a good structural stability and electrochemical performance.

The structural properties are explored by the ex-situ XRD patterns of Bare-LCO and Mg&P$_{0.02}$-LCO electrodes at different states of charge (Figure 4 (b) and Figure S11(b)). The Bragg diffraction peak shift with the charging/discharging declares a structural variation. It should be noted that Mg&P$_{0.02}$-LCO has a smaller structural change than Bare-LCO, which is evidenced by the restrained peak shift of Mg&P$_{0.02}$-LCO. The ex-situ Raman was further performed to reveal the structural evolution of both Bare-LCO and Mg&P$_{0.02}$-LCO cathode materials (Figure 4 (c) and Figure S11 (c)). It is discovered after one cycle, the peaks in the spectrum for 3.0V discharged Bare-LCO electrode are faded in intensity. While this is not observed in Mg&P$_{0.02}$-LCO.

For verifying the functions of Mg&P$_{0.02}$-LCO in restraining O release, DFT was used. The local structure and the oxygen vacancy formation in deep delithiation state is provided in Figure 4 (d)-(h) and Figure S12 and S13. The optimized structures of

pristine Bare-LCO and Mg&P$_{0.02}$-LCO cathode materials are shown in Figure S12. The band gap was reduced from 2.3 eV for Bare-LCO to 0.99 eV for Mg&P$_{0.02}$-LCO, which indicates a higher electronic conductivity in Mg&P$_{0.02}$-LCO. As shown in Figure 4(d) and (e), compared with a O_{2p} band center of -2.33 eV for Bare-LCO, Mg&P$_{0.02}$-LCO has a lower O_{2p} band center (-4.58 eV). The lower O_{2p} band center of Mg&P$_{0.02}$-LCO signifies an enhance ionicity[23]. It is reported that it restrains the oxygen redox and enhances the stability of oxygen framework.

In addition, the formation energies of oxygen vacancies in $Li_{0.4}CoO_2$($x \approx 0.4$, corresponding with charged 4.5V) and $Li_{0.26}CoO_2$($x \approx 0.26$ corresponding with charged 4.6V) were calculated as shown in Figure 4 (f)-(h). In Figure S13 (a)~(d), the optimized structures of Bare-LCO and Mg&P$_{0.02}$-LCO cathode materials in deep delithiation state are provided. The formation models of the oxygen vacancies are shown in Figure 4 (f) and (g). As shown in Figure 4 (h), Bare-LCO has a small formation energy of oxygen vacancies, which indicate that the lattice oxygen is not stable, especially at high delithiation. While the formation energy of oxygen vacancies for Mg&P$_{0.02}$-LCO is much larger, which indicates an enhanced O framework and restrained O reactions.

Conclusion

In summary, a controlled Mg^{2+} and $(PO_4)^{3-}$ co-doping strategy was used to regulate the structure of $LiCoO_2$. Li/Co anti-site is hence increased. Combined with advanced techniques, the underlying mechanisms is unraveled. The appropriate increase of the Li/Co anti-site defect inhibits the redox coupling of the cations, enhances the Co redox and reduces the O redox. The oxygen vacancies of the improved cathode at high

delithiation are restrained. These functions enhance the structural stability and inhibits oxygen escape. Furthermore, the $(PO_4)^{3-}$ doping also can stabilize oxygen-packed framework owing to a strong bond energy with the TM. The improved cathode delivers high capacities and maintains good long cycle capacity retentions with both the 4.5 and 4.6V voltage ceilings. This study provides some new insights into inhibiting the cationic redox coupling and improving the oxygen redox reversibility by adjusting the anti-site defects.

Acknowledgements

This work was supported by National Natural Science Foundation of China (Grant No. 11975238, 22005302 and 11575192), the Scientific Instrument Developing Project (Grant No. ZDKYYQ20170001), the Strategic Priority Research Program (Grant No. XDB28000000) and the International Partnership Program (Grant No. 211211KYSB20170060 and 211211KYSB20180020) of the Chinese Academy of Sciences, of the Chinese Academy of Sciences. This work was also supported by the Fundamental Research Funds for the Central Universities, the China Postdoctoral Science Foundation (2020M680648) and Shandong Weiqiao Pioneering Group Company Limited.

Conflict of interest The authors declare that they have no conflict of interest.

Reference

[1] a) H. Hafiz, K. Suzuki, B. Barbiellini, N. Tsuji, N. Yabuuchi, K. Yamamoto, Y. Orikasa, Y. Uchimoto, Y. Sakurai, H. Sakurai, A. Bansil, V. Viswanathan, *Nature* **2021**, *594*, 213; b) L. Yang, K. Yang, J. Zheng, K. Xu, K. Amine, F. Pan, *Chem. Soc. Rev*. **2020**, *49*, 4667.; c) S. L. Spence, A. Hu, M. Jiang, Z. Xu, Z. Yang, M. M. Rahman, L. Li, Y. S. Chu, X. Xiao, X. Huang, F. Lin, ACS Energy Lett. 2022, 7, 690.

[2] a) A. Manthiram, *Nat.Ccommun*. **2020**, *11*, 1550; b) Y. Kang, X. Guo, Z. Guo, J. Li, Y. Zhou, Z. Liang, C. Han, X. He, Y. Zhao, N. Tavajohi, B. Li, *J. Energy Chem*. **2021**, *62*, 538; c) J. Ahn, Y. Ha, R. Satish, R. Giovine, L. Li, J. Liu, C. Wang, R. J. Clement, R. Kostecki, W. Yang, G. Chen, *Adv. Energy Mater*. **2022**, *12*, 2200426. d) L. Ni, R. Guo, S. Fang, J. Chen, J. Gao, Y. Mei, S. Zhang, W. Deng, G. Zou, H. Hou, X. Ji, *eScience* **2022**, 2, 116.

[3] a) S. Mao, Z. Shen, W. Zhang, Q. Wu, Z. Wang, Y. Lu, *Adv. Sci*. **2022**, *9*, e2104841; b) X. Yang, C. Wang, P. Yan, T. Jiao, J. Hao, Y. Jiang, F. Ren, W. Zhang, J. Zheng, Y. Cheng, X. Wang, W. Yang, J. Zhu, S. Pan, M. Lin, L. Zeng, Z. Gong, J. Li, Y. Yang, *Adv. Energy Mater*. **2022**, *12*, 2200197.; c) S. D. Zhang, M. Y. Qi, S. J. Guo, Y. G. Sun, X. X. Tan, P. Z. Ma, J. Y. Li, R. Z. Yuan, A. M. Cao, L. J. Wan, *Small Methods* **2022**, *6*, e2200148.

[4] a) F.-E. Er-Rami, M. Duffiet, S. Hinkle, J. Auvergniot, M. Blangero, P.-E. Cabelguen, K. Song, F. Weill, C. Delmas, D. Carlier, *Chem. Mater*. **2022**, *34*, 4384.; b) W. Huang, Q. Zhao, M. Zhang, S. Xu, H. Xue, C. Zhu, J. Fang, W. Zhao, G. Ren, R. Qin, Q. Zhao, H. Chen, F. Pan, *Adv. Energy Mater*. **2022**, *12*, 2200813.

[5] a) W. Kong, J. Zhang, D. Wong, W. Yang, J. Yang, C. Schulz, X. Liu, *Angew. Chem*. **2021**, *60*, 27102; b) M. Yoon, Y. Dong, Y. Yoo, S. Myeong, J. Hwang, J. Kim, S. H. Choi, J. Sung, S. J. Kang, J. Li, J. Cho, *Adv. Funct. Mater*. **2019**, *30*, 1907903; c) Z. Zhu, H. Wang, Y. Li, R. Gao, X. Xiao, Q. Yu, C. Wang, I. Waluyo, J. Ding, A. Hunt, J. Li, *Adv. Mater*. **2020**, *32*, 2005182; d) A. Yano, N. Taguchi, H. Kanzaki, M. Shikano, H. Sakaebe, *J. Electrochem. Soc*. **2021**, *168*, 050517. e) J. Liu, J. Wang, Y. Ni, J. Liu, Y. Zhang, Y. Lu, Z. Yan, K. Zhang, Q. Zhao, F. Cheng, J. Chen, *Angew. Chem*. **2022**, 61, e202207000.

[6] a) X. Wang, Q. Wu, S. Li, Z. Tong, D. Wang, H. L. Zhuang, X. Wang, Y. Lu, *Energy Storage Mater*. **2021**, 37, 67-76; b) X. Tan, T. Zhao, L. Song, D. Mao, Y. Zhang, Z. Fan, H. Wang, W. Chu, *Adv. Energy Mater*. **2022**, 12, 2200008; c) X. Tan, D. Mao, T. Zhao, Y. Zhang, L. Song, Z. Fan, G. Liu, H. Wang, W. Chu, *Small* **2022**, 18, 2202143.

[7] a) J. Zhang, P. F. Wang, P. Bai, H. Wan, S. Liu, S. Hou, X. Pu, J. Xia, W. Zhang, Z. Wang, B. Nan, X. Zhang, J. Xu, C. Wang, *Adv. Mater*. **2022**, 34, e2108353; b) J. Xu, *Nanomicro. Lett*. **2022**, 14, 166.

[8] a) D. Ensling, G. Cherkashinin, S. Schmid, S. Bhuvaneswari, A. Thissen, W. Jaegermann, *Chem. Mater*. **2014**, *26*, 3948; b) B. Li, D. Xia, *Adv. Mater*. **2017**, *29*, 1701054.; c) A. Manthiram, A. Vadivel Murugan, A. Sarkar, T. Muraliganth, *Energy. Environ. Sci*. **2008**, *1*, 621.

[9] a) J. Li, C. Lin, M. Weng, Y. Qiu, P. Chen, K. Yang, W. Huang, Y. Hong, J. Li, M. Zhang, C. Dong,

W. Zhao, Z. Xu, X. Wang, K. Xu, J. Sun, F. Pan, *Nat. Nanotech*. **2021**, *16*, 599.; b) H. Zhang, H. Liu, L. F. J. Piper, M. S. Whittingham, G. Zhou, *Chem. Rev*. **2022**, *122*, 5641.; c) Y. Lyu, X. Wu, K. Wang, Z. Feng, T. Cheng, Y. Liu, M. Wang, R. Chen, L. Xu, J. Zhou, Y. Lu, B. Guo, *Adv. Energy Mater*. **2020**, *11*, 2000982.

[10] A. Fu, Z. Zhang, J. Lin, Y. Zou, C. Qin, C. Xu, P. Yan, K. Zhou, J. Hao, X. Yang, Y. Cheng, D.-Y. Wu, Y. Yang, M.-S. Wang, J. Zheng, *Energy Storage Mater*. **2022**, *46*, 406.

[11] W. Hu, Y. Chen, H. kou, Y. Wang, H. Wan, H. Li, *Ionics* **2022**, *28*, 3139.

[12] M. Sathiya, K. Ramesha, G. Rousse, D. Foix, D. Gonbeau, A. S. Prakash, M. L. Doublet, K. Hemalatha, J. M. Tarascon, *Chem. Mater*. **2013**, *25*, 1121.

[13] L. Wang, J. Ma, C. Wang, X. Yu, R. Liu, F. Jiang, X. Sun, A. Du, X. Zhou, G. Cui, *Adv. Sci*. **2019**, *6*, 1900355.

[14] a) J. Zhang, D. Zhou, W. Yang, J. Yang, L. Sun, G. Schumacher, X. Liu, *J. Electrochem. Soc*. **2019**, *166*, A4097; b) S.-J. Sim, S.-H. Lee, B.-S. Jin, H.-S. Kim, *J. Power Sources* **2021**, *481*, 229037.

[15] a) W. Kong, W. Yang, D. Ning, Q. Li, L. Zheng, J. Yang, K. Sun, D. Chen, X. Liu, *Sci. China Mater*. **2020**, *63*, 1703; b) R. Qi, J.-L. Shi, X.-D. Zhang, X.-X. Zeng, Y.-X. Yin, J. Xu, L. Chen, W.-G. Fu, Y.-G. Guo, L.-J. Wan, *Sci. China Chem*. **2017**, *60*, 1230; c) X. Liu, B. Ouyang, R. Hao, P. Liu, X. Fan, M. Zhang, M. Pan, W. Liu, K. Liu, *ChemElectroChem* **2022**, e20220609.

[16] a) X. Huang, D. Li, H. Huang, X. Jiang, Z. Yang, W. Zhang, *Nano Research* **2021**, *14*, 3531; b) Y.-M. Kang, Y.-I. Kim, M.-W. Oh, R.-Z. Yin, Y. Lee, D.-W. Han, H.-S. Kwon, J. H. Kim, G. Ramanath, *Energy. Environ. Sci*. **2011**, *4*, 4978; c) Q. Wei, R. H. DeBlock, D. M. Butts, C. Choi, B. Dunn, *Energy. Environ. Mater*. **2020**, *3*, 221.

[17] a) Q. Li, D. Zhou, L. Zhang, D. Ning, Z. Chen, Z. Xu, R. Gao, X. Liu, D. Xie, G. Schumacher, X. Liu, *Adv. Funct. Mater*. **2019**, *29*, 1806706; b) B. Li, H. Yan, J. Ma, P. Yu, D. Xia, W. Huang, W. Chu, Z. Wu, *Adv. Funct. Mater*. **2014**, *24*, 5112.

[18] a) P. F. Wang, H. R. Yao, T. T. Zuo, Y. X. Yin, Y. G. Guo, *Chem. Commun*. **2017**, *53*, 1957; b) S. Yanxia, H. Chunxi, S. Yue, Z. Jinbo, Z. Lijuan, L. Xiang, R. Xiufeng, D. Shengde, Z. Guotai, S. Chao, Z. Yuan, *J. Electrochem. Soc*. **2020**, *167*, 020522.

[19] a) H. Z. Zhang, Q. Q. Qiao, G. R. Li, X. P. Gao, *J. Mater. Chem. A* **2014**, *2*, 7454; b) G. Yang, K. Pan, F. Lai, Z. Wang, Y. Chu, S. Yang, J. Han, H. Wang, X. Zhang, Q. Li, *Chem. Eng. J*. **2021**, *421*, 129964.

[20] a) F. M. Wang, E. B. Chemere, W. C. Chien, C. L. Chen, C. C. Hsu, N. H. Yeh, Y. S. Wu, C. Khotimah,

K. W. Guji, L. Merinda, *ACS appl. Mater. interfaces* **2021**, *13*, 46703; b) X. Zheng, Y. Chen, W. Lai, P. Li, C. Ye, N. Liu, S. X. Dou, H. Pan, W. Sun, *Adv. Funct. Mater*. **2022**, *32*, 2200663.

[21] a) J.-N. Zhang, Q. Li, C. Ouyang, X. Yu, M. Ge, X. Huang, E. Hu, C. Ma, S. Li, R. Xiao, W. Yang, Y. Chu, Y. Liu, H. Yu, X.-Q. Yang, X. Huang, L. Chen, H. Li, *Nature Energy* **2019**, *4*, 594; b) R. A. House, J.-J. Marie, M. A. Pérez-Osorio, G. J. Rees, E. Boivin, P. G. Bruce, *Nature Energy* **2021**, *6*, 781.

[22] a) R. Sharpe, R. A. House, M. J. Clarke, D. Forstermann, J. J. Marie, G. Cibin, K. J. Zhou, H. Y. Playford, P. G. Bruce, M. S. Islam, *J. Am. Chem. Soc*. **2020**, *142*, 21799; b) Q. Li, D. Ning, D. Wong, K. An, Y. Tang, D. Zhou, G. Schuck, Z. Chen, N. Zhang, X. Liu, *Nat. Commun*. **2022**, 13, 1123.

[23] Q. Jacquet, A. Iadecola, M. Saubanere, H. Li, E. J. Berg, G. Rousse, J. Cabana, M. L. Doublet, J. M. Tarascon, *J. Am. Chem. Soc*. **2019**, *141*, 11452.